Full title: Eye-specific synaptic clustering through activity-dependent stabilization and punishment mechanisms in the developing visual system

Short title: Activity-dependent synaptic clustering underlies eye-specific competition

Author list: Chenghang Zhang[1] and Colenso M. Speer[1,*]

Author Affiliations: [1] Department of Biology, University of Maryland, College Park, Maryland, USA. 20742.

[*]Corresponding author

E-mail: cspeer@umd.edu (CS)

Abstract

Co-active synaptic connections are often spatially clustered to enable local dendritic computations underlying learning, memory, and basic sensory processing. In the mammalian visual system, retinal ganglion cell (RGC) axons converge to form clustered synaptic inputs for local signal integration in the dorsal lateral geniculate nucleus (dLGN) of the thalamus. Retinogeniculate synapse clustering is promoted by visual experience after eye-opening, but the earliest events in cluster formation and potential regulation by spontaneous retinal wave activity prior to visual experience are unknown. Here, using volumetric super-resolution single-molecule localization microscopy together with eye-specific labeling of developing retinogeniculate synapses in the mouse, we show that synaptic clustering is eye-specific and activity-dependent during the first postnatal week. We identified a subset of complex retinogeniculate synapses with larger presynaptic vesicle pools and multiple active zones that simultaneously promote the clustering of like-eye synapses (synaptic stabilization) and prohibit synapse clustering from the opposite eye (synaptic punishment). In mutant mice with disrupted spontaneous retinal wave activity, complex synapses form, but fail to drive eye-specific synaptic clustering and punishment seen in controls. These results highlight a role for spontaneous retinal activity in regulating eye-specific stabilization and punishment signals contributing to synaptic clustering in circuits essential for visual perception and behavior.

Introduction

A hallmark of neuronal computation is the formation of spatially clustered synaptic inputs to facilitate local computations within individual dendrites (1-3). Through linear and non-linear signal integration mechanisms, synaptic clusters play critical computational roles in learning, memory, and sensory processing underlying cognition and behavior (4-7). During circuit development, the formation of synaptic clusters is regulated by both spontaneous and sensory-driven neural activity that helps to stabilize or eliminate individual synapses to establish mature connectivity patterns (5, 6, 8).

A model example of activity-dependent synaptic cluster formation is the refinement of retinal inputs to the dorsal lateral geniculate nucleus (dLGN) of the thalamus (9). Electron microscopy (EM) reconstructions of the mouse dLGN reveal the convergence of retinal ganglion cell (RGC) inputs to form “complex” synaptic clusters known as glomeruli (10-13). Each individual glomerulus contains multiple RGC axon terminal boutons formed onto a dendritic branch of a dLGN relay neuron. Individual bouton structures vary from small terminals with a single active zone (AZ) to large and/or perforated synapses containing multiple AZs (10-13). These ultrastructural observations are supported by additional experimental results from transsynaptic (14) and Brainbow-based RGC labeling (11, 13), optogenetic stimulation of RGC axons (15, 16), and calcium imaging of retinogeniculate boutons (17) confirming the clustering of RGC inputs to relay neuron dendrites in the dLGN. Because individual glomeruli often receive inputs from multiple RGCs encoding either similar or distinct visual features (17), the

56 proper developmental wiring of RGC bouton clusters is critical for local dendritic
57 integration functions that drive visual spike responses in the adult brain.
58
59 Previous studies have shown that synaptic cluster development in neural circuits
60 depends upon spatiotemporally correlated synaptic activity that induces local
61 biochemical and mechanical signaling mechanisms to regulate synaptogenesis,
62 pruning, and plasticity (6, 18). In the developing retinogeniculate system, there are two
63 sources of correlated activity that could contribute to synaptic clustering: 1) visual
64 experience that drives topographic activation of neighboring RGCs and 2) spontaneous
65 retinal wave activity that correlates burst firing of neighboring RGCs prior to eye-
66 opening. Consistent with experience-dependent plasticity, retinogeniculate bouton
67 clustering increases after eye-opening (10, 13, 19) and visual deprivation reduces
68 clustering (19). However, these experience-dependent changes occur long after the
69 spontaneous activity-dependent segregation of eye-specific retinogeniculate axons prior
70 to eye-opening (20-22). Before photoreceptor-mediated visual onset, retinal waves
71 generate spatiotemporal correlations in RGC burst activity that are predicted to facilitate
72 Hebbian strengthening of co-active synapses (Butts et al., 2007) and promote eye-
73 specific synaptic clustering. Whether retinogeniculate synapse clustering begins prior to
74 eye-opening and is regulated by spontaneous retinal activity is unknown.
75
76 To address this question, we used volumetric super-resolution microscopy together with
77 anterograde tract tracing and immunohistochemical synaptic protein labeling to
78 investigate the development of clustered eye-specific synapses in the dLGN prior to the

onset of photoreceptor-mediated visual experience. During the first postnatal week, we identified a subpopulation of retinogeniculate synapses from both eyes-of-origin that contained larger presynaptic vesicle pools and multiple active zones (AZs). These “complex” synapses acted as loci for the clustering of synapses from the same eye (synaptic stabilization). At the same time, complex synapses of opposite eyes-of-origin showed a distance-dependent interaction that reduced synaptic clustering in an eye-specific manner during retinogeniculate competition (synaptic punishment). These patterns of synaptic stabilization and punishment were absent in a genetic mutant mouse line with disrupted stage II cholinergic retinal waves and abnormal eye-specific segregation. These results demonstrate that spontaneous retinal activity regulates retinogeniculate clustering prior to eye-opening and offer further support for the existence of non-cell-autonomous synaptic stabilization and punishment signals underlying eye-specific competition in the developing visual system.

Results

A unique set of complex synapses shows eye-specific differences during retinogeniculate segregation

To look for evidence of synaptic clustering during eye-specific segregation, we collected super-resolution imaging data in the dLGN of wild-type (WT) mice at three postnatal time points (P2, P4, and P8) (Fig 1A). We labeled eye-specific synapses by monocular injection of Alexa Fluor-conjugated cholera toxin subunit B tracer (CTB) together with immunostaining for presynaptic Bassoon, postsynaptic Homer1, and presynaptic vesicular glutamate transporter 2 (VGluT2) proteins (23). Using volumetric STochastic Optical Reconstruction Microscopy (STORM) (24), we collected separate image volumes (~45K μm^3 each) from three biological replicates at each developmental time point. To determine whether spontaneous retinal activity impacts synaptic clustering across the same time period, we performed identical experiments in a knockout mouse line lacking the beta 2 subunit of the nicotinic acetylcholine receptor (β2KO), which disrupts spontaneous cholinergic retinal wave activity, eye-specific axonal segregation, and retinogeniculate synapse development (20, 23, 25-33). Because eye-specific segregation is incomplete until P8 in the mouse, we limited our analysis to the future contralateral eye-specific region of the dLGN, which is reliably identified across all stages of postnatal development (Fig 1A, see also Materials and methods).

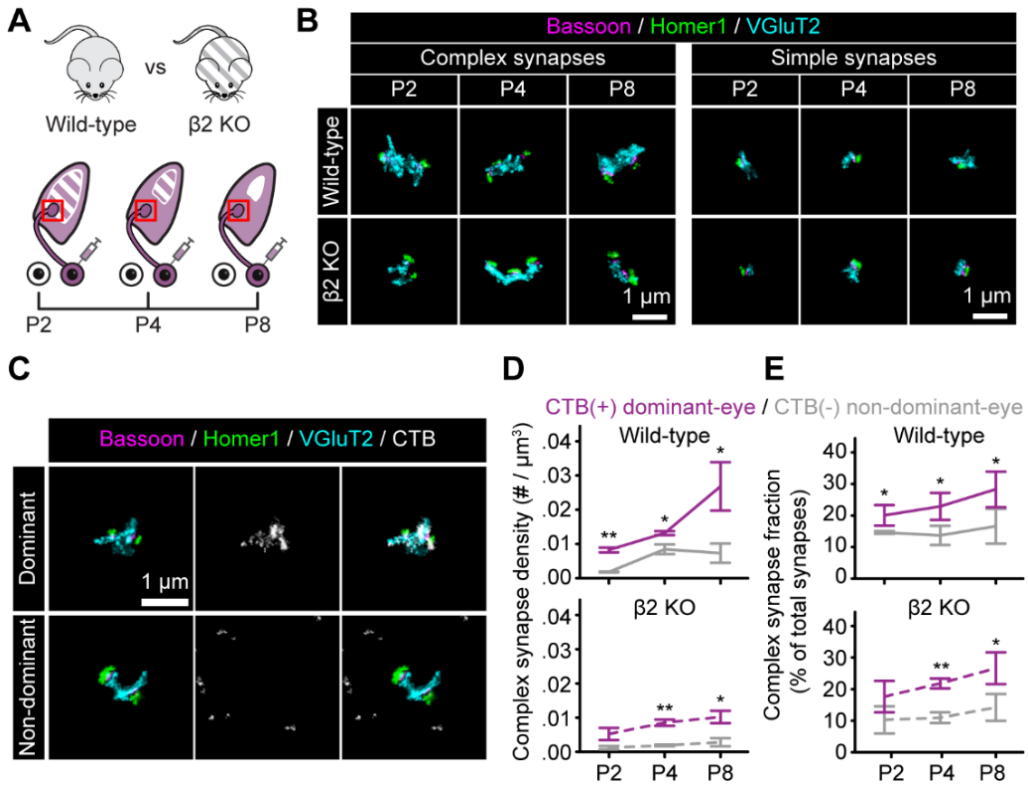

116

Fig 1. A unique set of complex synapses shows eye-specific differences during retinogeniculate segregation. (A) Experimental design: CTB-Alexa 488 was injected into the right eye of wild-type (WT) and β2KO mice. Tissue was collected from the left dLGN at P2, P4, and P8. The red squares indicate the STORM imaging regions. (B) Representative complex (left panels) and simple synapses (right panels) in WT (top panels) and β2KO mice (bottom panels) at each age. (C) Representative CTB(+) dominant-eye (top panels) and CTB(-) non-dominant-eye (bottom panels) complex synapses in a WT P8 sample, showing synaptic (left panels), CTB (middle panels), and merged immunolabels (right panels). (D) Eye-specific complex synapse density across development in WT (top panel) and β2KO mice (bottom panel). (E) Eye-specific complex synapse fraction across development in WT (top panel) and β2KO mice (bottom panel). In (D) and (E), error bars represent means ± SEMs. Statistical significance between CTB(+) and CTB(-) synapse measurements was assessed using one-way ANOVA. *: $p<0.05$, **: $p<0.01$. N=3 biological replicates for each age/genotype.

117

118

119 Across our dataset collected from different ages and genotypes, the enhanced
120 resolution of STORM images revealed distinct subtypes of retinogeniculate synapses
121 (S1A Fig). These included “complex” synapses characterized by the presence of
122 multiple (2-4) Bassoon(+) active zones (AZs) and greater VGluT2 signal, as well as
123 “simple” retinogeniculate synapses that were smaller and contained a single AZ (Fig 1B
124 and S1A Fig). To determine the eye-of-origin for each retinogeniculate synapse, we
125 measured the colocalization of CTB signal with VGluT2 (Fig 1C). By imaging in the
126 contralateral eye-specific region relative to the CTB-injected eye, we defined CTB(+)
127 VGluT2 clusters as “dominant-eye” synapses originating from the contralateral eye.
128 Conversely, CTB(-) VGluT2 clusters were classified as “non-dominant eye” synapses
129 originating from the ipsilateral eye (Fig 1C). Our previous work using binocular CTB
130 control injections confirmed the high efficiency of retinogeniculate synapse labeling by
131 anterograde tracing, thereby enabling accurate assignment of eye-specific synapses in
132 the mouse brain (23).
133
134 After assigning eye-of-origin to all retinogeniculate synapses, we measured the density
135 of complex and simple synapses from both eyes over development. In WT mice, the
136 density of CTB(+) dominant-eye complex synapses increased progressively from P2 to
137 P8 (Fig 1D, upper panel). In contrast, the density of CTB(-) non-dominant-eye complex
138 synapses increased from P2 to P4 and then decreased at P8 (Fig 1D, upper panel). The
139 density of simple synapses followed the same pattern (S1B Fig, upper panel) consistent
140 with the overall refinement of eye-specific synapses (23). In β2KO mice, the density of

141 both complex (Fig 1D, lower panel) and simple eye-specific synapses (S1B Fig, lower
142 panel) was reduced relative to controls at P4 and P8.
143
144 To further investigate complex synapse maturation, we measured the fraction of
145 complex synapses relative to the total synapse number over development. In WT mice,
146 the total fraction of dominant-eye complex synapses increased from ~20% at P2 to
147 ~29% at P8 while non-dominant-eye complex synapses remained constant between
148 ~14-17% across the same period (Fig 1E, upper panel). A similar pattern of eye-specific
149 complex synapse maturation was found in β2KO mice (Fig 1E, lower panel), showing
150 that relative proportions of complex versus simple synapses appeared normal despite
151 an overall reduction in total synapse density when spontaneous retinal activity was
152 disrupted (23).
153

154 Complex synapses undergo eye-specific vesicle pool 155 maturation

156 Each complex synapse could represent an individual, larger RGC bouton with multiple
157 active zones, or, alternatively, several clustered simple RGC boutons originating from
158 one or more presynaptic RGC axons (10, 12, 13). To distinguish these possibilities, we
159 compared the developmental changes in VGluT2 volume and active zone number for
160 complex versus simple synapses. In WT mice, both complex (Fig 2A, left panel) and
161 simple (Fig 2B, left panel) synapses showed developmental increases and eye-specific
162 differences in presynaptic VGluT2 volume. In WT complex synapses at P4, the median
163 dominant-eye VGluT2 cluster volumes were 372% larger than non-dominant-eye

164 VGluT2 clusters (Fig 2A, left panel). In contrast, β2KO mice showed a smaller
165 magnitude difference (110%) between eye-specific complex synapse VGluT2 volume at
166 the same time point (Fig 2A, right panel). In simple synapses at P4, the magnitudes of
167 eye-specific differences in VGluT2 volume were reduced to 135% (WT, Fig 2B, left
168 panel) and 41% (β2KO, Fig 2B, right panel). These results indicate that eye-specific
169 differences in vesicle pool size are more significant for complex synapses versus simple
170 synapses and that the maturation of both synapse types is regulated by spontaneous
171 retinal activity.

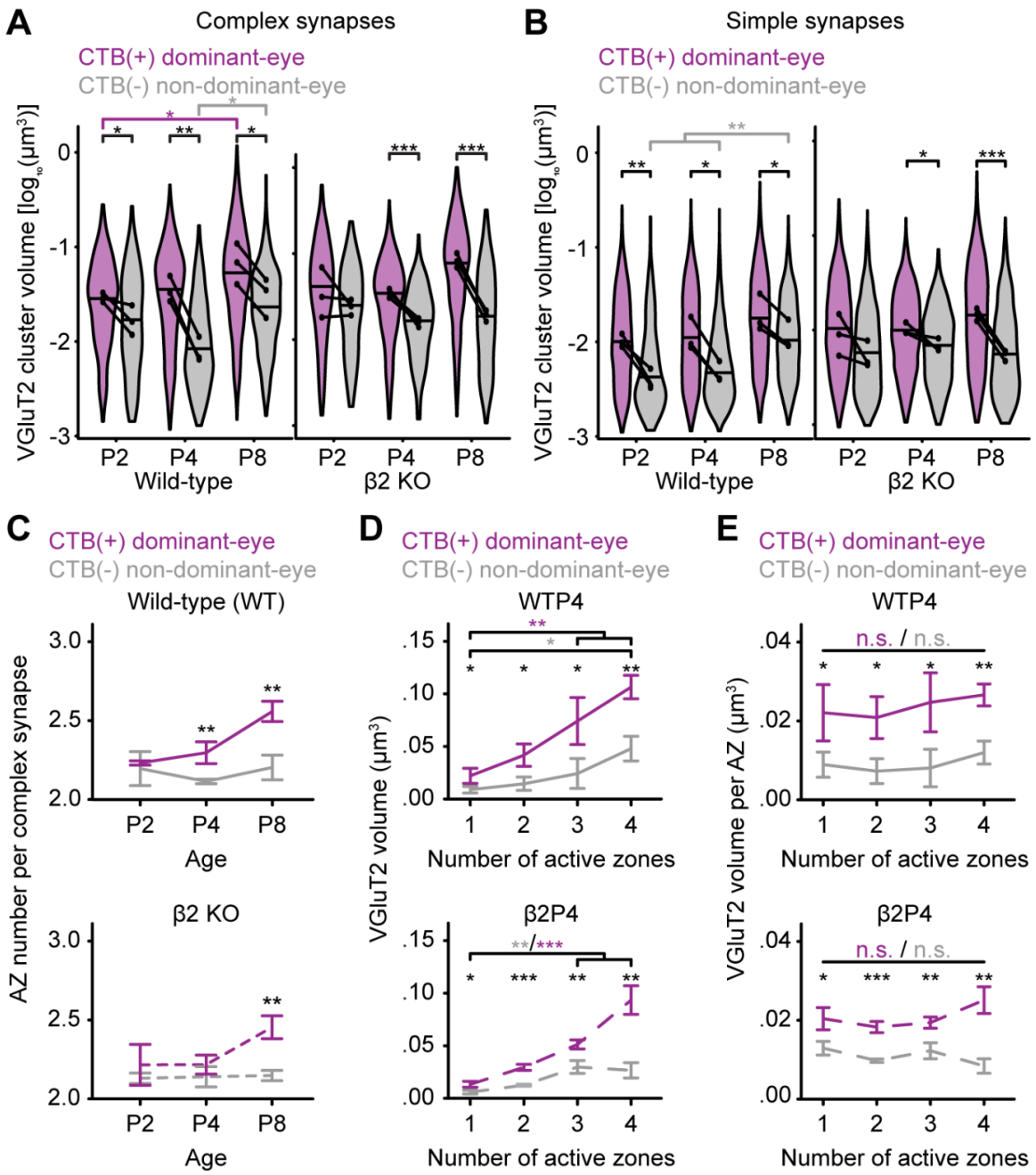
A
Complex synapses
CTB(+) dominant-eye
CTB(-) non-dominant-eye
VGluT2 cluster volume [log10(µm3)]
P2
P4
P8
Wild-type
β2 KO
B
Simple synapses
C
Wild-type (WT)
AZ number per complex synapse
Age
β2 KO
D
WTP4
β2P4
VGluT2 volume (µm3)
Number of active zones
E
n.s. / n.s.
VGluT2 volume per AZ (µm3)

172

Fig 2. Complex synapses undergo eye-specific vesicle pool maturation. (A) Violin plots showing the distribution of VGluT2 cluster volume for complex synapses in WT and β2KO mice at each age. The black dots represent the median value of each biological replicate (N=3) and the black horizontal lines represent the median value of all synapses. Black lines connect measurements of CTB(+) and CTB(-) populations from the same biological replicate. Statistical significance was determined using a mixed model ANOVA with a post hoc Bonferroni test. Black asterisks indicate eye-specific differences and colored asterisks indicate differences across time points. (B) Violin plots similar to (A) show the distribution of VGluT2 cluster volume for simple synapses in WT and β2KO mice at each age. (C) Average number of active zones (AZs = individual bassoon clusters) per complex synapse in WT (top panel) and β2KO mice (bottom panel). (D) VGluT2 cluster volume as a function of AZ number for all synapses in WT P4 samples (top panel) and β2KO P4 samples (bottom panel). (E) Average VGluT2 cluster volume per AZ for all synapses in WT P4 samples (top panel) and β2KO P4 samples (bottom panel). In (C-E), error bars represent means ± SEMs from N=3 biological replicates. Statistical significance was assessed using one-way ANOVA with a post hoc Tukey's test. Black asterisks indicate eye-specific differences and colored asterisks indicate differences between simple (1 AZ) and complex (>1 AZ) synapses. "n.s." indicates no significance between simple and complex synapses. In all panels, *: $p<0.05$, **: $p<0.01$, ***: $p<0.001$.

173 We next measured the number of Bassoon clusters in each complex synapse and
174 asked whether the corresponding VGluT2 cluster volume was consistent with a
175 summation of VGluT2 volume from multiple simple synapses. In both WT (Fig 2C, top
176 panel) and β2KO mice (Fig 2C, bottom panel), complex synapses were associated with
177 an average of 2-3 Bassoon clusters in the first postnatal week. The average number of
178 AZs in CTB(+) dominant-eye complex synapses increased from P2-P8, while CTB(-)
179 non-dominant-eye synapses did not add AZs during this period (Fig 2C). For CTB(+)
180 dominant-eye synapses in both WT and β2KO mice, the size of the vesicle pool was

181 positively correlated with the number of AZs (Fig 2D, S2A/B Figs). This correlation was
182 also present in CTB(-) non-dominant-eye synapses, but with a smaller magnitude.
183 Dividing the total presynaptic VGluT2 volume by the AZ number showed that simple and
184 complex synapses had an equivalent presynaptic vesicle volume associated with each
185 AZ (Fig 2E, S2C/D Figs). This suggests that complex synapses in the first postnatal
186 week are comprised of several simple RGC synapses each with similar VGluT2 volume
187 (putative nascent glomeruli). This conclusion is further supported by EM data showing
188 that individual synaptic terminals in the P7 mouse dLGN are commonly associated with
189 a single AZ (10).
190

191 Complex synapses are loci for synaptic clustering

192 Previous studies support the hypothesis that eye-specific competition is achieved
193 through stabilization and strengthening of co-active dominant-eye RGC inputs together
194 with punishment and elimination of non-dominant-eye inputs (34-36). Within this
195 context, complex synapses with multiple presynaptic release sites may drive strong
196 postsynaptic responses and the induction of non-cell-autonomous stabilization and/or
197 elimination signals that regulate synaptic cluster development (37-39). To investigate
198 whether complex synapses contribute to synaptic clustering, we measured the fraction
199 of eye-specific simple synapses located near like-eye complex synapses and compared
200 this to a randomized simple synapse distribution (Fig 3A-C). Simple synapses were
201 considered nearby if their weighted centroids were within 1.5 μm of a complex synapse
202 edge (Fig 3A, S3 Fig). For CTB(+) dominant-eye projections in WT mice, simple
203 synapses showed non-random clustering near complex synapses, which increased

204 progressively over development (Fig 3B, middle panel). In contrast, when searching for
205 CTB(-) non-dominant-eye simple synapses nearby CTB(+) dominant-eye complex
206 synapses, we found no evidence for synaptic clustering (S3A Fig, middle panel). These
207 results indicate that CTB(+) dominant-eye complex synapses stabilize the local
208 formation of like-eye-type simple synapses.

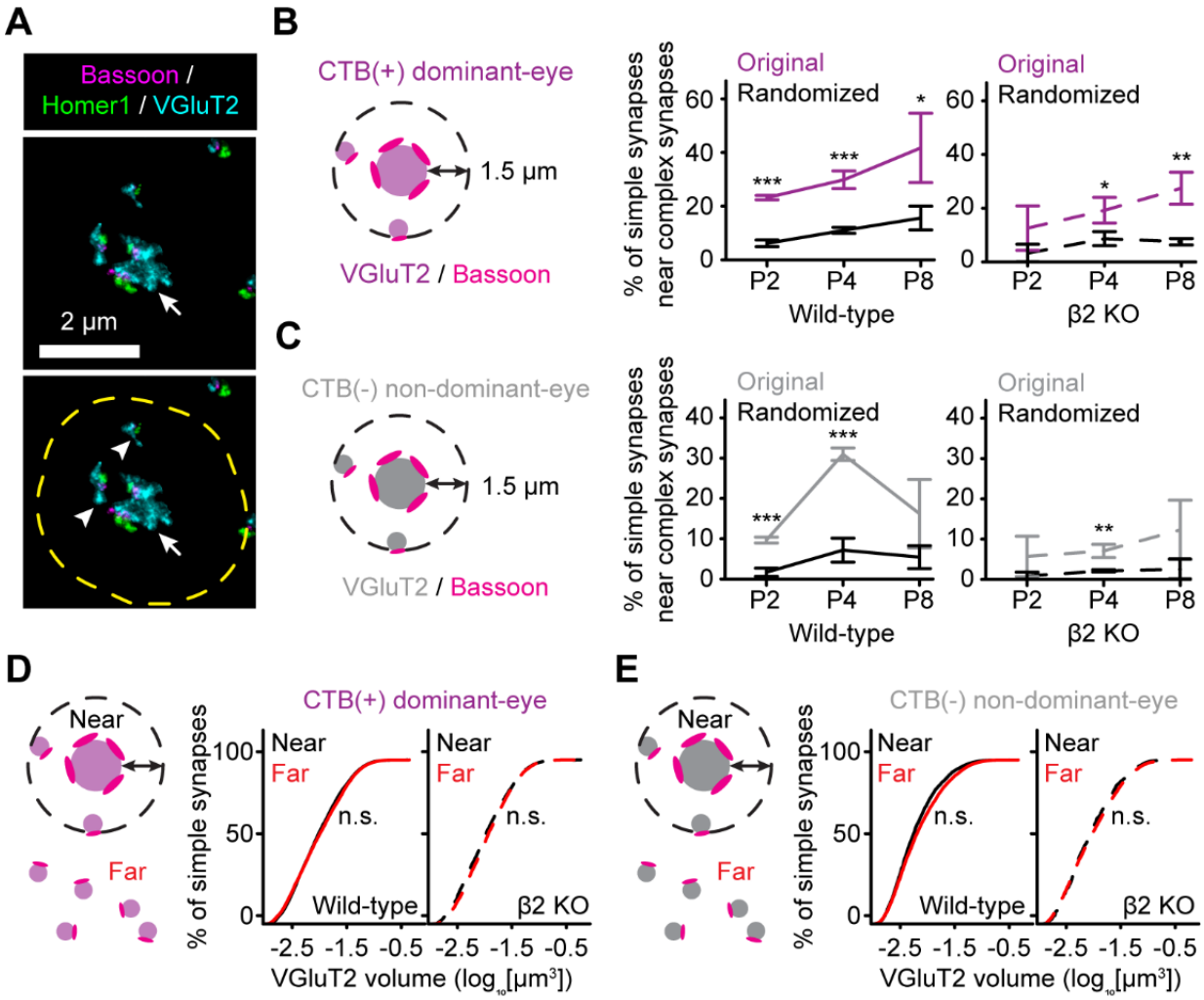

209

Fig 3. Complex synapses are loci for synaptic clustering. (A) A representative complex synapse in a WT P8 dLGN (arrow) with nearby simple synapses (arrowheads) clustered within 1.5 μm (dashed yellow ring). (B) The fraction of CTB(+) dominant-eye simple synapses near like-eye complex synapses (cartoon) across development in WT (middle panel) and β2KO mice (right panel). Colored lines show the measured distributions and black lines show results of a randomized simple synapse distribution within the sample imaging volume. (C) Same as in (B) showing results for CTB(-) non-dominant-eye simple synapses near like-eye complex synapses. In B/C, a one-way ANOVA was used to test the statistical significance between original and randomized data. Error bars represent means ± SEMs. *: $p<0.05$; **: $p<0.01$; ***: $P<0.001$. (D) Cumulative distribution of simple synapse VGluT2 volume for CTB(+) dominant-eye simple synapses near (<1.5 μm, black lines) or far from (>1.5 μm, red lines) like-eye complex synapses. (E) Same as in (D) showing the cumulative distribution of simple synapse VGluT2 volume for CTB(-) non-dominant-eye simple synapse relative to like-eye complex synapses. The distributions in (D/E) show merged data across all developmental ages. A nonparametric Kolmogorov-Smirnov test was used for statistical analysis. "n.s." indicates no significant difference between near and far simple synapse distributions.

Similarly, for CTB(-) non-dominant-eye complex synapses in WT mice, we observed a significant increase in the clustering of like-eye CTB(-) non-dominant-eye simple synapses nearby from P2 to P4 (Fig 3C, middle panel). Subsequently, the fraction of clustered simple synapses decreased from P4 to P8, reaching a level similar to randomized data (Fig 3C, middle panel). This increase in clustering coincides with ipsilateral RGC axon synaptogenesis (23) and demonstrates that ipsilateral CTB(-) complex synapses promote local synaptogenesis despite being in the future contralateral eye-specific territory. However, after the close of eye-specific competition at P8, clustered CTB(-) simple synapses were eliminated, indicating that CTB(-)

221 complex synapses failed to stabilize nearby simple synapses during eye-specific
222 competition. This effect was not due to an overall loss of complex synapses as the
223 CTB(-) complex synapse fraction was consistent across the first postnatal week (Fig
224 1E). Just as we found for CTB(+) dominant-eye complex synapses, CTB(-) non-
225 dominant-eye complex synapses showed no selective stabilization of simple synapses
226 from the opposite eye (S3B Fig, middle panel).
227
228 In β2KO mice, CTB(+) dominant-eye complex synapses also stabilized nearby like-eye
229 simple synapses, although the effect size was reduced relative to controls (Fig 3B, right
230 panel). Similarly, CTB(-) non-dominant-eye complex synapses in β2KO mice failed to
231 stabilize like-eye simple synapses to the level seen in controls (Fig 3C, right panel). As
232 we observed in control mice, complex synapses of either eye did not selectively
233 stabilize opposite eye-synapses in β2KO mice (S3A/B Fig, lower panels). Together,
234 these results suggest that while local synapse stabilization mechanisms are at least
235 partially maintained in β2KO mice, defects in spontaneous retinal activity reduce eye-
236 specific synaptic clustering.
237
238 Based on our independent findings of eye-specific differences in vesicle pool volume
239 (Fig 2 A/B) and non-random synapse clustering around complex synapses (Fig 3 A-C),
240 we hypothesized that complex synapses might also regulate the vesicle pool size of
241 nearby simple synapses as a mechanism contributing to presynaptic maturation. To test
242 this, we divided the population of simple synapses into two groups: those that were
243 within a 1.5 μm radius of a like-eye complex synapse ('near') and those that were at any

244 distance >1.5 μm ('far'). When comparing the vesicle pool volumes between near and
245 far simple synapse groups across all ages and genotypes, we found no significant
246 differences for either dominant-eye or non-dominant-eye simple synapses (Fig 3D/E,
247 displays the data merged for all time points). This result shows that activity-dependent
248 synapse stabilization mechanisms do not impact simple synapse vesicle pool size.
249

250 Complex synapses mediate distance-dependent synaptic 251 stabilization and punishment underlying eye-specific 252 competition

253 RGC axon refinement is a dynamic process involving branch stabilization and
254 elimination based upon the relative activity patterns among neighboring inputs (37, 40).
255 Axonal remodeling is partially regulated by synaptic transmission (41) and the induction
256 of non-cell-autonomous stabilization and punishment signals (38, 39, 42). Although the
257 precise mechanisms of axonal stabilization and punishment are not fully understood, it
258 is likely that non-cell-autonomous signals operate at a local scale through direct cell-cell
259 interactions or diffusible paracrine factors. Based on our observation that CTB(-) non-
260 dominant-eye simple synapses initially cluster around like-eye complex synapses and
261 were eliminated during eye-specific competition (Fig 3C), we hypothesized that CTB(-)
262 synapses may be punished by nearby CTB(+) dominant-eye complex synapses in a
263 distance-dependent manner.
264

265 To test this hypothesis, we first examined whether the size of CTB(-) non-dominant-eye
266 complex synapses is affected by their spatial proximity to CTB(+) dominant-eye
267 complex synapses (Fig 4A/B). For each CTB(-) complex synapse, we measured the
268 vesicle pool volume (Fig 4A, P4 data as an example) and AZ number (Fig 4B) as a
269 function of each synapse's distance to the nearest CTB(+) complex synapse. We found
270 no correlation between presynaptic properties and inter-eye complex synapse distances
271 across all ages in both WT mice (Fig 4 A/B, left panels) and β2KO mice (Fig 4A/B, right
272 panels) (P2/P8 data not shown). These findings align with our earlier discovery that
273 simple synapse vesicle pool volume is unaffected by proximity to complex synapses
274 (Fig 3C), suggesting that presynaptic protein organization is not influenced by
275 mechanisms governing synaptic clustering.

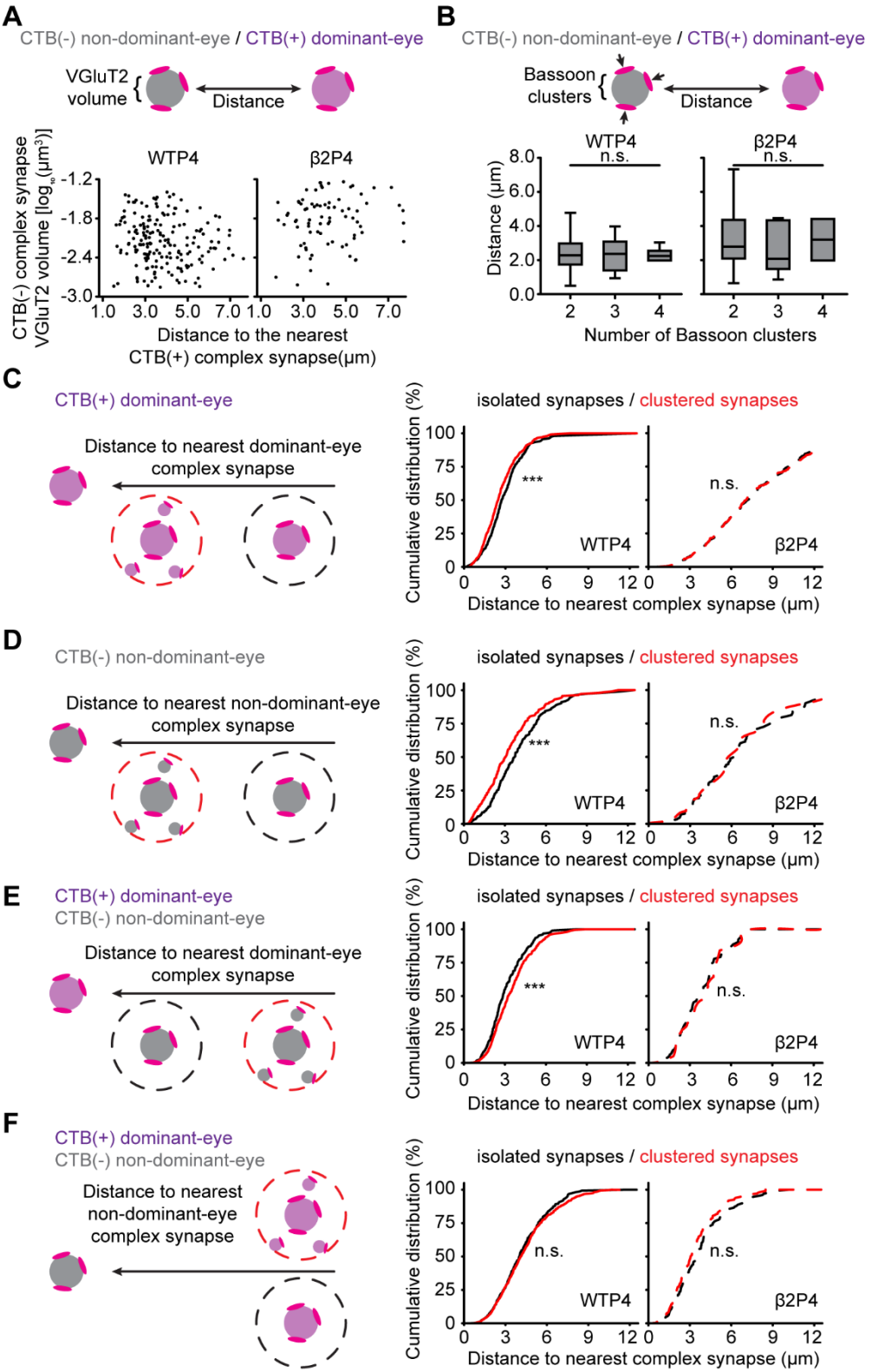
A
CTB(-) non-dominant-eye / CTB(+) dominant-eye
VGluT2 volume
Distance
WTP4
β2P4
CTB(-) complex synapse VGluT2 volume [log10(μm3)]
-1.2
-1.8
-2.4
-3.0
1.0 3.0 5.0 7.0 1.0 3.0 5.0 7.0
Distance to the nearest CTB(+) complex synapse(μm)
B
CTB(-) non-dominant-eye / CTB(+) dominant-eye
Bassoon clusters
Distance
WTP4
n.s.
β2P4
n.s.
Distance (μm)
8.0
6.0
4.0
2.0
0.0
2 3 4 2 3 4
Number of Bassoon clusters
C
CTB(+) dominant-eye
Distance to nearest dominant-eye complex synapse
isolated synapses / clustered synapses
Cumulative distribution (%)
100
75
50
25
0
***
WTP4
n.s.
β2P4
0 3 6 9 12 0 3 6 9 12
Distance to nearest complex synapse (μm)
D
CTB(-) non-dominant-eye
Distance to nearest non-dominant-eye complex synapse
isolated synapses / clustered synapses
Cumulative distribution (%)
100
75
50
25
0
***
WTP4
n.s.
β2P4
0 3 6 9 12 0 3 6 9 12
Distance to nearest complex synapse (μm)
E
CTB(+) dominant-eye
CTB(-) non-dominant-eye
Distance to nearest dominant-eye complex synapse
isolated synapses / clustered synapses
Cumulative distribution (%)
100
75
50
25
0
***
WTP4
n.s.
β2P4
0 3 6 9 12 0 3 6 9 12
Distance to nearest complex synapse (μm)
F
CTB(+) dominant-eye
CTB(-) non-dominant-eye
Distance to nearest non-dominant-eye complex synapse
isolated synapses / clustered synapses
Cumulative distribution (%)
100
75
50
25
0
n.s.
WTP4
n.s.
β2P4
0 3 6 9 12 0 3 6 9 12
Distance to nearest complex synapse (μm)

276

277

Fig 4. Complex synapses mediate distance-dependent synaptic stabilization and punishment underlying eye-specific competition. (A) VGluT2 volume of CTB(-) non-dominant-eye complex synapses relative to their distance to the nearest CTB(+) dominant-eye complex synapse in a WT P4 sample (left panel) and a β2KO P4 sample (right panel). Each black dot represents one synapse. (B) Distributions of distances between CTB(-) non-dominant-eye complex synapses and their nearest CTB(+) dominant-eye complex synapse separated by the number of AZs within each CTB(-) complex synapse in WT P4 samples (left panel) and β2KO P4 samples (right panel). The median value is indicated by the horizontal line within the box, while the box boundaries represent quartile values. The whiskers represent the maximum and minimum values. A mixed model ANOVA was used to perform statistical tests. "n.s." indicates no significance differences. (C) Cumulative distributions of distances between CTB(+) dominant-eye complex synapses and their nearest CTB(+) dominant-eye complex synapse (cartoon) in WT P4 samples (left panel) and β2KO P4 samples (right panel). Red lines indicate clustered complex synapses with nearby (<1.5 μm) simple synapses and black lines indicate isolated complex synapses with no nearby simple synapses. (D) Same presentation as in (C), showing distances between CTB(-) complex synapses. (E) Same presentation as in (C), showing distances between CTB(-) non-dominant-eye complex synapses and their nearest CTB(+) dominant-eye complex synapse (cartoon). (F) Same presentation as in (C), showing distances between CTB(+) dominant-eye complex synapses and the nearest CTB(-) non-dominant-eye complex synapse. For C-F, nonparametric Kolmogorov-Smirnov tests were used for statistical comparisons. "***" indicates $p<0.001$, while "n.s." indicates no significant differences.

Next, we investigated whether complex synapses influence synaptic clustering around other nearby complex synapses in a distance-dependent manner. For this analysis, we categorized eye-specific complex synapses into two groups: complex synapses with nearby (< 1.5 μm) simple synapses from the same eye (referred to as “clustered”), and complex synapses with no nearby simple synapses (referred to as “isolated”). We then

284 measured the distance between each complex synapse and its closest complex
285 synapses from each eye-of-origin (Fig 4 C-F).
286
287 In WT mice at P4, we found that clustered CTB(+) dominant-eye complex synapses
288 were closer to other CTB(+) complex synapses compared to isolated CTB(+) synapses,
289 indicating a synaptic stabilization effect (Fig 4C, left panel). Similarly, clustered CTB(-)
290 non-dominant-eye complex synapses were closer to the nearest CTB(-) complex
291 synapse compared to isolated CTB(-) complex synapses (Fig 4D, left panel). These
292 distance-dependent relationships were not observed when complex synapse positions
293 of the target eye were randomized (S4A/B Fig). These findings indicate that complex
294 synapses from both eyes are more likely to stabilize like-eye-type simple synapses
295 when they are in closer proximity to other complex synapses from the same eye. The
296 stabilization effect of CTB(+) complex synapse clustering persisted until P8 (S4C Fig,
297 left panel). However, by P8, CTB(-) complex synapse stabilization was not observed
298 (S4D Fig, right panel), consistent with synapse elimination and a loss of CTB(-)
299 clustering by this time point (Fig 3C). Furthermore, distance-dependent effects on
300 synaptic clustering at P4 were only observed in WT mice and not in β2KO mice (Fig 4
301 C/D, right panels; S4E/F Fig, shows P8 β2KO data).
302
303 To look for evidence of competitive interactions between synapses from the two eyes,
304 we next measured the distances between clustered and isolated CTB(-) non-dominant
305 eye complex synapses and the closest CTB(+) dominant-eye complex synapse (Fig
306 4E). In WT mice at P4, we observed that isolated CTB(-) non-dominant-eye complex

307 synapses were closer to the nearest CTB(+) dominant-eye complex synapse compared
308 to clustered CTB(-) synapses (Fig 4E, left panel), consistent with an opposite-eye
309 punishment signal. Similar to our findings on synaptic stabilization, this punishment
310 effect was not observed in β2KO mice (Fig 4E, right panel) or when complex synapse
311 positions of the target eye were randomized (S4A/B Fig).
312
313 Lastly, we compared the distances between clustered versus isolated CTB(+) dominant-
314 eye synapses with respect to CTB(-) non-dominant-eye complex synapses and we
315 found no differences in WT mice (Fig 4F, left panel) or β2KO mice (Fig 4F, right panel).
316 This suggests that complex synapses from the non-dominant-eye do not exert a
317 punishment effect on synapses from the dominant-eye (Fig 4F). Together, these results
318 demonstrate that complex synapses contribute to eye-specific competition through
319 activity-dependent stabilization and punishment mechanisms that act locally (within ~6
320 μm) to regulate synaptic clustering.
321

322 # Discussion

323 Relay neurons of the dLGN function as crucial hubs for the integration of RGC inputs
324 within eye-specific synaptic clusters to drive spike output to the primary visual cortex. In
325 this study, we used volumetric super-resolution microscopy together with eye-specific
326 synaptic immunolabeling to show that 1) eye-specific synaptic clustering begins during
327 retinogeniculate refinement prior to eye-opening, 2) synaptic clustering is regulated by a
328 subpopulation of complex synapses with large vesicle pools and multiple AZs, 3)
329 complex synapses regulate clustering through distance-dependent stabilization of like-

330 eye synapses and punishment of opposite-eye synapses, and 4) eye-specific synaptic
331 clustering relies on normal spontaneous retinal wave activity during the first postnatal
332 week. These results advance our understanding of the developmental timeline of
333 retinogeniculate glomerulus development and suggest that spontaneous neural activity
334 regulates synaptic stabilization and punishment signals underlying competitive synaptic
335 refinement in the developing visual system.
336
337 Previous anatomical studies have demonstrated the maturation of retinogeniculate
338 glomeruli through the progressive clustering of RGC boutons following eye-opening in
339 mice (10, 13, 19). This process is visual experience-dependent and is partly disrupted
340 by sensory deprivation (late dark-rearing) (19). At maturity, retinogeniculate clusters are
341 primarily eye-specific and contain very few, weak synapses from the non-dominant eye
342 within each eye-specific region (14, 16). Our STORM images reveal that eye-specific
343 synaptic clustering emerges prior to eye-opening, during the period of eye-specific
344 competition regulated by stage II cholinergic retinal waves. This clustering is marked by
345 the development of a subset of complex synapses that contain a greater number of
346 synaptic vesicles and AZs (putative clustered RGC terminal boutons). These synapses
347 differ from simple synapses (isolated RGC terminals) that have fewer vesicles and a
348 single active zone.
349
350 Since our STORM images did not include a membrane stain, we were unable to identify
351 the boundaries of individual RGC terminals. Therefore, it remains unclear whether
352 complex synapses represent multiple RGC boutons or single terminals with multiple

353 AZs. However, several lines of evidence suggest that complex synapses likely consist
354 of two or more small RGC terminals, each with a single AZ. First, we found that the
355 vesicle pool volume in complex synapses is proportional to the number of associated
356 AZs, with each AZ having a comparable vesicle pool size to that of simple synapses.
357 Second, the developmental increase in complex synapse vesicle pool volume matches
358 that of simple synapses. Third, previous electron microscopy (EM) imaging data in the
359 P7 mouse dLGN shows that synaptic profiles are small and mainly associated with a
360 single AZ (10). Larger retinogeniculate terminals containing several AZs are observed
361 later in development after eye-opening (10, 13).
362
363 Compared to mature synaptic glomeruli (~ 6 μm diameter), complex synapses formed
364 during the first postnatal week are significantly smaller (~1 μm diameter). This suggests
365 that further aggregation and convergence of RGC inputs are required for the maturation
366 of complex synapses into bona fide glomeruli. Consistent with this, we found that
367 complex synapses acted as local hubs for the clustering of additional like-eye-type
368 simple synapses. The radius of simple synapse clustering around complex synapses
369 was in the range of ~ 3-4 μm, indicating that these clustered simple synapses may
370 serve as the substrate for glomerulus maturation.
371
372 In the adult dLGN, bouton clustering facilitates the convergence of RGC inputs
373 representing similar visual features (e.g. direction of motion) and the integration of
374 parallel visual channels carried by unique RGC mosaics (12, 14, 17). Retinal waves
375 drive co-activation of synaptic transmission in boutons from neighboring RGCs, which

376 may support the development of clustered synaptic inputs to relay neurons. Consistent
377 with this, pharmacological and genetic disruptions of cholinergic retinal wave
378 propagation decrease direction selective responses in postsynaptic neurons in the
379 superior colliculus (43). Our STORM images revealed that in β2KO mice with disrupted
380 retinal waves, complex synapses were formed and showed a development increase in
381 vesicle pool volume and AZ number similar to WT mice (Fig 2). However, the clustering
382 of simple synapses around complex synapses was reduced, though not eliminated (Fig
383 3 B/C), in β2KO mice. Since retinal waves persist in β2KO mice (31-33), a residual level
384 of correlated activity between adjacent RGC synapses may be sufficient to promote
385 synaptic clustering. In the future, it will be of interest to investigate how correlated
386 synaptic activity impacts local clustering using pharmacological or optogenetic
387 manipulations to reduce or enhance RGC correlations in the developing retina (44-47).
388
389 While studying the spatial relationships between complex synapses, we observed
390 increased clustering of dominant-eye inputs (stabilization) and decreased clustering of
391 non-dominant-eye inputs (punishment) depending on the distance between eye-specific
392 complex synapses. Synaptic clustering was more likely to occur around complex
393 synapses that were nearby other complex synapses from the same eye (within ~ 6 μm).
394 This finding is consistent with the presence of non-cell-autonomous signals that regulate
395 eye-specific axonal stabilization (37, 38, 42). In addition to mechanisms that stabilize
396 axon branches, eye-specific projections also undergo competitive refinement and
397 axonal retraction mediated by punishment signals. Neurotransmission plays a crucial
398 role in these mechanisms as shown by genetic deletions of VGluT2 or RIM1 proteins

399 from ipsilaterally-projecting RGCs (41, 48). These deletions decrease presynaptic
400 vesicle release and prevent contralateral RGC axon retraction from the ipsilateral eye-
401 specific territory in the dLGN (41, 48). One downstream mediator of synaptic
402 punishment is JAK2 kinase, which is phosphorylated in less active synapses (39).
403 Similar to VGluT2 and RIM1 deletion phenotypes, over-expression of a dominant-
404 negative mutant JAK2 lacking kinase activity prevents axon retraction in transfected
405 RGCs during eye-specific competition (39).
406
407 Our super-resolution images show that synapse clustering is less likely to occur around
408 non-dominant-eye complex synapses when they were located nearby dominant-eye
409 complex synapses (a competitive punishment effect). This finding is consistent with
410 previous studies of bulk axonal remodeling and highlights the role of synaptic
411 punishment in axonal refinement phenotypes. In β2KO mice at P4, we did not find
412 evidence of distance-dependent effects on synaptic clustering (either stabilization or
413 punishment), indicating that spontaneous retinal activity regulates eye-specific synaptic
414 clustering mechanisms at a local microcircuit scale (within ~ 6 μm). A possible
415 mechanism underlying this effect is the activity-dependent development of functional
416 presynaptic terminals. We previously found that β2KO mice fail to develop eye-specific
417 differences in vesicle recruitment to the active zone, which are normally present in WT
418 mice as early as P2 (23). This effect is accompanied by an overall reduction in the
419 number of retinogeniculate synapses in the β2KO mouse (23). In the current study, we
420 found that complex synapses show greater eye-specific differences in presynaptic
421 vesicle pool volume compared to simple synapses and that these eye-specific

422 differences are significantly reduced in β2KO mice. Altogether, these results are
423 consistent with a model in which spontaneous retinal activity regulates presynaptic
424 development and vesicle release probability, which is required for the induction of local
425 stabilization and punishment signals that govern eye-specific synapse clustering.
426
427 Our results in the developing retinogeniculate system bear similarities to the
428 development of synaptic clusters in other circuits. During the refinement of the
429 neuromuscular junction (NMJ), individual myocytes are initially innervated by multiple
430 motor neuron axons that form intermingled synapses (49, 50). Subsequently, NMJ
431 terminals undergo competitive refinement, where connections from a single motor axon
432 are elaborated and strengthened, while competing axons are eliminated (51, 52).
433 Similar to our findings on eye-specific complex synapse development, competition at
434 the developing NMJ is also dependent on inter-synaptic distance, with motor axons
435 losing connections that are in closer proximity to their competing synapses (49, 50).
436 This process is activity-dependent, and blocking synaptic activity with pharmacological
437 or genetic methods biases competition and leads to elimination of the silenced inputs
438 (53, 54). Interestingly, competing motor axon outputs show differences in presynaptic
439 release probability at early stages of development, suggesting that biases in presynaptic
440 release may underlie competition (55), possibly through the induction of local
441 stabilization and punishment signals (52).
442
443 While the molecular mechanisms regulating synaptic competition at the NMJ are not
444 well understood, additional insights have been gained from studies of the developing

445 hippocampus. Synaptic clustering onto hippocampal pyramidal neurons is activity-
446 dependent and is blocked by chronic application of TTX or NMDA-receptor antagonists
447 (56). Activation of NMDA receptors by co-active inputs triggers postsynaptic calcium-
448 induced calcium-release and spreading calcium signals that regulate the maturation of
449 clustered synapses (57). While co-active synapses are strengthened by spontaneous
450 activity, synapses with asynchronous activity undergo synaptic depression, which is
451 blocked by disruptions of proBDNF/P75^{NTR} signaling (58). Similarly, the clustering of co-
452 active inputs is prevented by manipulations of BDNF-TrkB signaling and matrix
453 metalloproteinase 9 (MMP9), a proteinase that converts proBDNF to mature BDNF (59).
454 Together, these findings suggest a model in which postsynaptic activation by co-active
455 inputs drives local spreading intracellular calcium signaling, leading to proBDNF
456 release. Extracellular proBDNF is then cleaved by MMP9 to induce BDNF-TrkB
457 signaling, which stabilizes locally synchronized synapses and promotes cluster
458 maturation (59). At the same time, proBDNF may weaken asynchronous synapses
459 through P75^{NTR} activation (58). Relating these neurotrophic mechanisms to visual
460 system development, a computational model that incorporates BDNF-mediated synaptic
461 refinement suggests that correlations in retinal waves are sufficient to induce local
462 synaptic clustering contributing to orientation selectivity in cortical neurons (60).
463 Supporting a role for correlated spontaneous activity in synaptic refinement for the
464 computation of directional motion, disruptions of retinal wave activity through
465 pharmacological and genetic approaches reduce direction-selective responses in the
466 mouse superior colliculus (43).
467

468 Although the molecular mechanisms underlying the clustering of eye-specific
469 retinogeniculate inputs are still unknown, our STORM imaging results provide
470 anatomical support for the existence of local signaling factors that mediate non-cell-
471 autonomous interactions, which underlie both synaptic stabilization and punishment.
472 These factors may induce direct signaling between presynaptic RGC axon terminals or,
473 alternatively, initiate postsynaptic responses that lead to reverse cell-cell signaling or
474 the release of diffusible retrograde factors that stabilize and eliminate synapses based
475 on input timing. JAK2/STAT signaling has been identified as one downstream regulator
476 of synaptic punishment (39), which helps narrow the search for specific upstream
477 induction signals in future experiments. It will also be of special interest to further
478 investigate the eye-specific induction of glial-associated phagocytic signaling pathways
479 that prune weak synapses during eye-specific segregation (61-63).
480

481 # Materials and methods:

482 The raw imaging data in this paper were previously reported (23). Materials and
483 methods below are adapted from this work.
484

485 ## Animals

486 Wild-type C57BL/6J mice used in this study were purchased from the Jackson
487 Laboratory (Stock Number 000664). β2KO mice were a generous gift of Dr. Michael C.
488 Crair (Yale School of Medicine). All experimental procedures were performed in
489 accordance with an animal study protocol approved by the Institutional Animal Care and
490 Use Committee (IACUC) at the University of Maryland. Neonatal male and female mice

491 were used interchangeably for all experiments. Tissue from biological replicates (N=3
492 animals) was collected for each age (P2/P4/P8) from each genotype (WT and β2KO)
493 (18 animals total). Primers used for genotyping β2KO mice include: forward primer
494 CAGGCGTTATCCACAAAGACAGA; reverse primer
495 TTGAGGGGAGCAGAACAGAATC; mutant reverse primer
496 ACTTGGGTTTGGGCGTGTTGAG (64, 65).
497

498 ## Eye injections

499 Intraocular eye injections were performed one day before tissue collection. Briefly, mice
500 were anesthetized by inhalant isoflurane and sterile surgical spring scissors were used
501 to gently part the eyelid to expose the corneoscleral junction. A small hole was made in
502 the eye using a sterile 34-gauge needle and ~0.5 µl of cholera toxin subunit B
503 conjugated with Alexa Fluor 488 (CTB-488, ThermoFisher Scientific, Catalogue
504 Number: C34775) diluted in 0.9% sterile saline was intravitreally pressure-injected into
505 the right eye using a pulled-glass micropipette coupled to a Picospritzer (Parker
506 Hannifin).
507

508 ## dLGN tissue preparation

509 Animals were deeply anesthetized with ketamine/xylazine and transcardially perfused
510 with 5-10 mls of 37°C 0.9% sterile saline followed by 10 mls of room temperature 4%
511 EM Grade paraformaldehyde (PFA, Electron Microscopy Sciences) in 0.9% saline.
512 Brains were embedded in 2.5% agarose and sectioned in the coronal plane at 100 µm
513 using a vibratome. From the full anterior-posterior series of dLGN sections (~6-8

514 sections) we selected the central two sections for staining in all biological replicates.
515 These sections were morphologically consistent with Figures 134-136 (5.07-5.31 mm)
516 of the postnatal day 6 mouse brain from Paxinos, et al., “Atlas of the developing mouse
517 brain” Academic Press, 2020 (66). Selected sections were postfixed in 4% PFA for 30
518 minutes at room temperature and then washed for 30-40 minutes in 1X PBS. The dLGN
519 was identified by the presence of CTB-488 signals using a fluorescence dissecting
520 microscope. A circular tissue punch (~500 μm diameter) containing the dLGN was
521 microdissected from each section using a blunt-end needle. A small microknife cut was
522 made at the dorsal edge of the dLGN which, together with the CTB-488 signal, enabled
523 us to identify the dLGN orientation during image acquisition.
524

525 Immunohistochemistry

526 We used a serial-section single-molecule localization imaging approach to prepare
527 samples and collect super-resolution fluorescence imaging volumes as previously
528 described (24). dLGN tissue punches were blocked in 10% normal donkey serum
529 (Jackson ImmunoResearch, Catalogue Number: 017-000-121) with 0.3% Triton X-100
530 (Sigma-Aldrich Inc.) and 0.02% sodium azide (Sigma-Aldrich Inc.) diluted in 1X PBS for
531 2-3 hours at room temperature and then incubated in primary antibodies for ~72 hours
532 at 4°C. Primary antibodies used were Rabbit anti-Homer1 (Synaptic Systems,
533 Catalogue Number: 160003, 1:100) to label postsynaptic densities (PSDs), mouse anti-
534 Bassoon (Abcam, Catalogue Number AB82958, 1:100) to label presynaptic active
535 zones (AZs), and guinea pig anti-VGluT2 (Millipore, Catalogue Number AB251-I, 1:100)
536 to label presynaptic vesicles. Following primary antibody incubation, tissues were

537 washed in 1X PBS for 6 x 20 minutes at room temperature and incubated in secondary
538 antibody solution overnight for ~36 hours at 4°C. The secondary antibodies used were
539 donkey anti-rabbit IgG (Jackson ImmunoResearch, Catalogue Number 711-005-152,
540 1:100) conjugated with Dy749P1 (Dyomics, Catalogue Number 749P1-01) and Alexa
541 Fluor 405 (ThermoFisher, Catalogue Number: A30000), donkey anti-mouse IgG
542 (Jackson ImmunoResearch, Catalogue Number 715-005-150, 1:100) conjugated with
543 Alexa Fluor 647 (ThermoFisher, Catalogue Number: A20006) and Alexa Fluor 405, and
544 donkey anti-guinea pig IgG (Jackson ImmunoResearch, Catalogue Number 706-005-
545 148, 1:100) conjugated with Cy3b (Cytiva, Catalogue Number: PA63101). Tissues were
546 washed 6 x 20 minutes in 1X PBS at room temperature after secondary antibody
547 incubation.
548

549 Postfixation, dehydration, and embedding in epoxy resin

550 Tissue embedding was performed as previously described (24). Tissues were postfixed
551 with 3% PFA + 0.1% GA (Electron Microscopy Sciences) in PBS for 2 hours at room
552 temperature and then washed in 1X PBS for 20 minutes. To plasticize the tissues for
553 ultrasectioning, the tissues were first dehydrated in a graded dilution series of 100%
554 ethanol (50%/70%/90%/100%/100% EtOH) for 15 minutes each at room temperature
555 and then immersed in a series of epoxy resin/100% EtOH exchanges (Electron
556 Microscopy Sciences) with increasing resin concentration (25% resin/75% ethanol; 50%
557 resin/50% ethanol; 75% resin/25% ethanol; 100% resin; 100% resin) for 2 hours each.
558 Tissues were transferred to BEEM capsules (Electron Microscopy Sciences) that were
559 filled with 100% resin and polymerized for 16 hours at 70°C.

560

561 ## Ultrasectioning

562 Plasticized tissue sections were cut using a Leica UC7 ultramicrotome at 70 nm using a
563 Histo Jumbo diamond knife (DiATOME). Chloroform vapor was used to reduce
564 compression after cutting. For each sample, ~100 sections were collected on a
565 coverslip coated with 0.5% gelatin and 0.05% chromium potassium (Sigma-Aldrich Inc.),
566 dried at 60 degrees for 25 minutes, and protected from light prior to imaging.

567

568 ## Imaging chamber preparation

569 Coverslips were chemically etched in 10% sodium ethoxide for 5 minutes at room
570 temperature to remove the epoxy resin and expose the dyes to the imaging buffer for
571 optimal photoswitching. Coverslips were then rinsed with ethanol and dH_2O. To create
572 fiducial beads for flat-field and chromatic corrections, we mixed 715/755nm and
573 540/560nm, carboxylate-modified microspheres (Invitrogen, Catalogue Numbers F8799
574 and F8809, 1:8 ratio respectively) to create a high-density fiducial marker and then
575 further diluted the mixture at 1:750 with Dulbecco's PBS to create a low-density bead
576 solution. Both high- and low-density bead solutions were spotted on the coverslip (~0.7
577 ul each) for flat-field and chromatic aberration correction respectively. Excess beads
578 were rinsed away with dH2O for 1-2 minutes. The coverslip was attached to a glass
579 slide with double-sided tape to form an imaging chamber. The chamber was filled with
580 STORM imaging buffer (10% glucose, 17.5μM glucose oxidase, 708nM catalase, 10mM
581 MEA, 10mM NaCl, and 200mM Tris) and sealed with epoxy.

582

583 ## Imaging setup

584 Imaging was performed using a custom single-molecule super-resolution imaging
585 system. The microscope contained low (4x/10x air) and high (60x 1.4NA oil immersion)
586 magnitude objectives mounted on a commercial frame (Nikon Ti-U) with back optics
587 arranged for oblique incident angle illumination. We used continuous-wave lasers at
588 488nm (Coherent), 561nm (MPB), 647nm (MPB), and 750nm (MPB) to excite Alexa
589 488, Cy3B, Alexa 647, and Dy749P1 dyes respectively. A 405 nm cube laser
590 (Coherent) was used to reactivate Dy749P1 and Alexa647 dye photoswitching. The
591 microscope was fitted with a custom pentaband/pentanotch dichroic filter set and a
592 motorized emission filter wheel. The microscope also contained an IR laser-based focus
593 lock system to maintain optimal focus during automatic image acquisition. Images were
594 collected on 640*640-pixel region of an sCMOS camera (ORCA-Flash4.0 V3,
595 Hamamatsu Photonics) with a pixel size of ~155 nm.
596

597 ## Automated image acquisition

598 Fiducials and tissue sections on the coverslip were imaged using the low magnification
599 objective (4X) to create a mosaic overview of the specimen. Beads/sections were then
600 imaged at high-magnification (60X) to select regions of interest (ROIs) in the Cy3B and
601 Alexa 488 channels. Before final image acquisition, laser intensities and the incident
602 angle were adjusted to optimize photoswitching for STORM imaging and utilize the full
603 dynamic range of the camera for conventional imaging.
604

605 Low-density bead images were taken in 16 partially overlapping ROIs. 715/755nm
606 beads were excited using 750 nm light and images were collected through Dy749P1
607 and Alexa 647 emission filters. 540/560nm beads were excited using a 488 nm laser
608 and images were collected through Alexa 647, Cy3B, and Alexa 488 emission filters.
609 These fiducial images were later used to generate a non-linear warping transform to
610 correct chromatic aberration. Next, ROIs within each tissue section were imaged at
611 conventional (diffraction-limited) resolution in all four-color channels sequentially.
612
613 Following conventional image acquisition, a partially overlapping series of 9 images
614 were collected in the high-density bead field for all 4 channels (Dy749P1, Alexa 647,
615 Cy3B, and Alexa 488). These images were later used to perform a flat-field image
616 correction of non-uniform laser illumination across the ROIs. Another round of bead
617 images was taken as described above in a different ROI of the low-density bead field.
618 These images were later used to confirm the stability of chromatic offsets during
619 imaging. All ROIs within physical sections were then imaged by STORM for Dy749P1
620 and Alexa 647 channels. Images were acquired using a custom progression of
621 increasing 405nm laser intensity to control single-molecule switching. 8000 frames of
622 Dy749P1 channel images were collected (60 Hz imaging) followed by 12000 frames of
623 Alexa 647 channel images (100 Hz). In a second imaging pass, the same ROIs were
624 imaged for Cy3B and Alexa 488 channels, each for 8000 frames (60 Hz).
625
626 We imaged the ipsilateral and contralateral ROIs separately in each physical section of
627 the dLGN. For consistency of ROI selection across biological replicates at each age, we

628 identified the dorsal-ventral (DV) axis of the dLGN and selected ROIs within the center
629 (core region) at 2/5 (ipsilateral ROI) and 4/5 (contralateral ROI) of the full DV length.
630

631 Image processing

632 Single-molecule localization was performed using a previously described DAOSTORM
633 algorithm (67) modified for use with sCMOS cameras (68). Molecule lists were rendered
634 as 8-bit images with 15.5 nm pixel size where each molecule is plotted as an intensity
635 distribution with an area reflecting its localization precision. Low-density fiducial images
636 were used for chromatic aberration correction. We localized 715/755 beads in Dy749P1
637 and Alexa 647 channels, and 540/560 beads in Alexa 647, Cy3B, and Alexa 488
638 channels. A third-order polynomial transform map was generated by matching the
639 positions of each bead in all channels to the Alexa 647 channel. The average residual
640 error of bead matching was <15 nm for all channels. The transform maps were applied
641 to both 4-color conventional and STORM images. Conventional images were upscaled
642 (by 10X) to match the STORM image size. The method to align serial sections was
643 previously described (24). STORM images were first aligned to their corresponding
644 conventional images by image correlation. To generate an aligned 3D image stack from
645 serial sections, we normalized the intensity of all Alexa 488 images and used these
646 normalized images to generate both rigid and elastic transformation matrices for all four-
647 color channels of both STORM and conventional data. The final image stack was then
648 rotated and cropped to exclude incompletely imaged edge areas. Images of the
649 ipsilateral regions were further cropped according to CTB-488 signals to exclude
650 contralateral areas.

651

652 ## Cell body filter

653 The aligned STORM images had non-specific labeling of cell bodies in Dy749P1 and
654 Alexa 647 channels corresponding to Homer1 and Bassoon immunolabels. To limit
655 synaptic cluster identification to the neuropil region we identified cell bodies based on
656 their Dy749P1 signal and excluded these regions from further image processing.
657 STORM images were convolved with a Gaussian function (σ=140 nm) and then
658 binarized using the lower threshold of a two-level Otsu threshold method. We located
659 connected components in the thresholded images and generated a mask based on
660 components larger than e^{11} voxels. Because cell body clusters were orders of
661 magnitude larger than synaptic clusters, the cell body filter algorithm was robust to a
662 range of size thresholds. The mask was applied to images of all channels to exclude
663 cell body areas.

664

665

666

667 ## Eye-specific synapse identification and quantification

668 To correct for minor variance in image intensity across physical sections, we normalized
669 the pixel intensity histogram of each section to the average histogram of all sections.
670 Image histograms were rescaled to make full use of the 8-bit range. Using a two-level
671 Otsu threshold method, the conventional images were thresholded into three classes: a
672 low-intensity background, low-intensity signals above the background representing non-

673 synaptic labeling, and high-intensity signals representing synaptic structures. The
674 conventional images were binarized by the lower two-level Otsu threshold, generating a
675 mask for STORM images to filter out background signals. STORM images were
676 convolved with a Gaussian function (σ= 77.5 nm) and thresholded using the higher two-
677 level Otsu threshold. Following thresholding, connected components were identified in
678 three dimensions using MATLAB 'conncomp' function. A watershedding approach was
679 applied to split large clusters that were improperly connected. Clusters were kept for
680 further analysis only if they contained aligned image information across two or more
681 physical sections. We also removed all edge synapses from our analysis by excluding
682 synapses that did not have blank image data on all adjacent sides.
683
684 To distinguish non-specific immunolabeling from true synaptic signals, we quantified two
685 parameters for each cluster: cluster volume and cluster signal density calculated by the
686 ratio of within-cluster pixels with positive signal intensity in the raw STORM images.
687 Two separate populations were identified in 2D histograms plotted from these two
688 parameters. We manually selected the population with higher volumes and signal
689 densities representing synaptic structures. To test the robustness of the manual
690 selection, we performed multiple repeated measurements of the same data and
691 discovered a between-measurement variance of <1% (data not shown).
692
693 To identify paired pre- and postsynaptic clusters, we first measured the centroid-
694 centroid distance of each cluster in the Dy749P1 (Homer1) and Alexa 647 (Bassoon)
695 channels to the closest cluster in the other channel. We next quantified the signal

696 intensity of each opposing synaptic channel within a 140 nm shell surrounding each
697 cluster. A 2D histogram was plotted based on the measured centroid-centroid distances
698 and opposing channel signal densities of each cluster. Paired clusters with closely
699 positioned centroids and high intensities of apposed channel signal were identified
700 using the OPTICS algorithm. In total we identified 49,414 synapses from WT samples (3
701 samples each at P2/P4/P8, 9 total samples) and 33,478 synapses in $\beta2^{-/-}$ mutants (3
702 samples each at P2/P4/P8, 9 total samples). Retinogeniculate synapses were identified
703 by pairing Bassoon (Alexa 647) clusters with VGluT2 (Cy3B) clusters using the same
704 method as pre/post-synaptic pairing. Synapses from the right eye were identified by
705 pairing VGluT2 clusters with CTB (Alexa 488) clusters. The volume of each cluster
706 reflected the total voxel volume of all connected voxels, and the total signal intensity
707 was a sum of voxel intensity within the volume of the connected voxels.
708

709 Complex synapse identification and quantification

710 To determine whether an eye-specific VGluT2 cluster is a complex synapse or a simple
711 synapse, we measured the number of active zones (defined by individual Bassoon
712 clusters) associated with each VGluT2 cluster in the dataset. A 3D shell was extended
713 140 nm from the surface voxels of each VGluT2 cluster and any Bassoon clusters that
714 fell within the shell were considered to be associated with the target VGluT2 cluster.
715 The number of active zones (AZs) associated with each VGluT2 cluster was then
716 measured. VGluT2 clusters associated with more than 1 AZ were defined as complex
717 synapses, while those associated with only 1 AZ were defined as simple synapses.
718

719 Quantification of complex and simple synapse VGluT2 cluster volume was performed
720 using the "regionprops" function in MATLAB, which provided the voxel size and
721 weighted centroid of each VGluT2 cluster. The search for simple synapses adjacent to
722 complex synapses (synaptic clustering analysis) was conducted using a similar search
723 approach as for associated Bassoon clusters, with expansion shell sizes ranging from 1
724 μm to 4 μm from the surface voxels of each complex synapse. The main figures in the
725 study utilized an expansion size of 1.5 μm. An eye-specific simple synapse was
726 considered to be near a complex synapse if its weighted centroid fell within the
727 expanded region.
728

729 ## Quantification and Statistical Analysis

730 Statistical analysis was performed using SPSS. Plots were generated by SPSS or R
731 (ggplot2). Statistical details are presented in the figure legends. For all measurements in
732 this paper, we analyzed N = 3 biological replicates (individual mice) for each genotype
733 (WT and β2KO) at each age (P2, P4, and P8). Cluster densities, synapse AZ number,
734 average VGluT2 cluster volume, and all fraction measurements were presented as
735 mean ± SEM values in line plots and were compared by one-way ANOVA tests with a
736 post-hoc Tukey's test when there were more than 2 factors. Nonparametric
737 Kolmogorov-Smirnov tests were used in all cumulative histogram comparisons. We
738 used a linear mixed model to compare VGluT2 cluster volumes (Fig 2) and the distance
739 measurements in Fig 4B. For VGluT2 cluster volume comparisons, the age or eye-of-
740 origin was the fixed main factor and biological replicate IDs were nested random factors.
741 In distance measurement comparisons, the complex synapse AZ number was the fixed

742 main factor and biological replicate IDs were nested random factors. Pairwise
743 comparisons among main factor groups were performed by a post-hoc Bonferroni's test.
744 In violin plots, each violin showed the distribution of grouped data from all biological
745 replicates from the same condition. Each black dot represents the median value of each
746 biological replicate and the horizontal black line represents the group median. Black
747 lines connect measurements of CTB(+) and CTB(-) populations from the same
748 biological replicate. Asterisks in all figures indicate statistical significance: *P<0.05,
749 **P<0.01, ***P<0.001.
750

751 # Acknowledgements:

752 We thank Dr. Michael C. Crair for generously sharing the β2KO mouse line
753 used in this work.
754

755 # Author contributions:

756 Conceptualization, C.Z. and C.M.S.; data curation, C.Z. and C.M.S.;
757 formal analysis, C.Z. and C.M.S.; funding acquisition, C.M.S.; investigation,
758 C.Z. and C.M.S.; methodology, C.Z. and C.M.S.; project administration,
759 C.Z. and C.M.S.; resources, C.Z. and C.M.S.; software, C.Z.
760 and C.M.S.; supervision, C.M.S.; validation, C.Z. and C.M.S.; visualization,
761 C.Z. and C.M.S.; writing – original draft preparation, C.Z. and C.M.S.; writing –
762 review & editing, C.Z. and C.M.S.
763

764 # References:

765 1. Rall W. Electrophysiology of a dendritic neuron model. Biophys J. 1962;2(2 Pt 2):145-67.

766 2. Mel B, editor The Clusteron: Toward a Simple Abstraction for a Complex Neuron1991

767 1991: Morgan-Kaufmann.

768 3. Poirazi P, Mel BW. Impact of active dendrites and structural plasticity on the memory

769 capacity of neural tissue. Neuron. 2001;29(3):779-96.

770 4. Mel BW, Schiller J, Poirazi P. Synaptic plasticity in dendrites: complications and coping

771 strategies. Curr Opin Neurobiol. 2017;43:177-86.

772 5. Leighton AH, Lohmann C. The Wiring of Developing Sensory Circuits-From Patterned

773 Spontaneous Activity to Synaptic Plasticity Mechanisms. Front Neural Circuits. 2016;10:71.

774 6. Winnubst J, Lohmann C. Synaptic clustering during development and learning: the why,

775 when, and how. Front Mol Neurosci. 2012;5:70.

776 7. Kastellakis G, Poirazi P. Synaptic Clustering and Memory Formation. Front Mol Neurosci.

777 2019;12:300.

778 8. Kirchner JH, Gjorgjieva J. Emergence of synaptic organization and computation in

779 dendrites. 2022;28(1):21-30.

780 9. Bickford ME. Synaptic organization of the dorsal lateral geniculate nucleus. Eur J

781 Neurosci. 2019;49(7):938-47.

782 10. Bickford ME, Slusarczyk A, Dilger EK, Krahe TE, Kucuk C, Guido W. Synaptic development

783 of the mouse dorsal lateral geniculate nucleus. J Comp Neurol. 2010;518(5):622-35.

784 11. Hammer S, Monavarfeshani A, Lemon T, Su J, Fox MA. Multiple Retinal Axons Converge

785 onto Relay Cells in the Adult Mouse Thalamus. Cell Rep. 2015;12(10):1575-83.

786 12. Morgan JL, Berger DR, Wetzel AW, Lichtman JW. The Fuzzy Logic of Network
787 Connectivity in Mouse Visual Thalamus. Cell. 2016;165(1):192-206.
788 13. Monavarfeshani A, Stanton G, Van Name J, Su K, Mills WA, Swilling K, et al. LRRTM1
789 underlies synaptic convergence in visual thalamus. Elife. 2018;7:e33498.
790 14. Rompani SB, Mullner FE, Wanner A, Zhang C, Roth CN, Yonehara K, et al. Different
791 Modes of Visual Integration in the Lateral Geniculate Nucleus Revealed by Single-Cell-Initiated
792 Transsynaptic Tracing. Neuron. 2017;93(4):767-76 e6.
793 15. Litvina EY, Chen C. Functional Convergence at the Retinogeniculate Synapse. Neuron.
794 2017;96(2):330-8 e5.
795 16. Bauer J, Weiler S, Fernholz MHP, Laubender D, Scheuss V, Hubener M, et al. Limited
796 functional convergence of eye-specific inputs in the retinogeniculate pathway of the mouse.
797 Neuron. 2021;109(15):2457-68 e12.
798 17. Liang L, Fratzl A, Goldey G, Ramesh RN, Sugden AU, Morgan JL, et al. A Fine-Scale
799 Functional Logic to Convergence from Retina to Thalamus. Cell. 2018;173(6):1343-55 e24.
800 18. Pulikkottil VV, Somashekar BP, Bhalla US. Computation, wiring, and plasticity in synaptic
801 clusters. Curr Opin Neurobiol. 2021;70:101-12.
802 19. Hong YK, Park S, Litvina EY, Morales J, Sanes JR, Chen C. Refinement of the
803 retinogeniculate synapse by bouton clustering. Neuron. 2014;84(2):332-9.
804 20. Muir-Robinson G, Hwang BJ, Feller MB. Retinogeniculate axons undergo eye-specific
805 segregation in the absence of eye-specific layers. J Neurosci. 2002;22(13):5259-64.

806 21. Godement P, Salaün J, Imbert M. Prenatal and postnatal development of
807 retinogeniculate and retinocollicular projections in the mouse. J Comp Neurol.
808 1984;230(4):552-75.
809 22. Jaubert-Miazza L, Green E, Lo FS, Bui K, Mills J, Guido W. Structural and functional
810 composition of the developing retinogeniculate pathway in the mouse. Vis Neurosci.
811 2005;22(5):661-76.
812 23. Zhang C, Yadav S, Speer CM. The synaptic basis of activity-dependent eye-specific
813 competition. Cell Rep. 2023;42(2):112085.
814 24. Vatan T, Minehart JA, Zhang C, Agarwal V, Yang J, Speer CM. Volumetric super-
815 resolution imaging by serial ultrasectioning and stochastic optical reconstruction microscopy in
816 mouse neural tissue. STAR Protocols. 2021;2(4):100971.
817 25. Xu HP, Burbridge TJ, Chen MG, Ge X, Zhang Y, Zhou ZJ, et al. Spatial pattern of
818 spontaneous retinal waves instructs retinotopic map refinement more than activity frequency.
819 Dev Neurobiol. 2015;75(6):621-40.
820 26. Xu HP, Burbridge TJ, Ye M, Chen M, Ge X, Zhou ZJ, et al. Retinal Wave Patterns Are
821 Governed by Mutual Excitation among Starburst Amacrine Cells and Drive the Refinement and
822 Maintenance of Visual Circuits. J Neurosci. 2016;36(13):3871-86.
823 27. Xu HP, Furman M, Mineur YS, Chen H, King SL, Zenisek D, et al. An instructive role for
824 patterned spontaneous retinal activity in mouse visual map development. Neuron.
825 2011;70(6):1115-27.

826 28. Rossi FM, Pizzorusso T, Porciatti V, Marubio LM, Maffei L, Changeux JP. Requirement of
827 the nicotinic acetylcholine receptor beta 2 subunit for the anatomical and functional
828 development of the visual system. Proc Natl Acad Sci U S A. 2001;98(11):6453-8.
829 29. Grubb MS, Rossi FM, Changeux JP, Thompson ID. Abnormal functional organization in
830 the dorsal lateral geniculate nucleus of mice lacking the beta 2 subunit of the nicotinic
831 acetylcholine receptor. Neuron. 2003;40(6):1161-72.
832 30. Dhande OS, Hua EW, Guh E, Yeh J, Bhatt S, Zhang Y, et al. Development of single
833 retinofugal axon arbors in normal and beta2 knock-out mice. J Neurosci. 2011;31(9):3384-99.
834 31. Sun C, Warland DK, Ballesteros JM, van der List D, Chalupa LM. Retinal waves in mice
835 lacking the beta2 subunit of the nicotinic acetylcholine receptor. Proc Natl Acad Sci U S A.
836 2008;105(36):13638-43.
837 32. Stafford BK, Sher A, Litke AM, Feldheim DA. Spatial-temporal patterns of retinal waves
838 underlying activity-dependent refinement of retinofugal projections. Neuron. 2009;64(2):200-
839 12.
840 33. Bansal A, Singer JH, Hwang BJ, Xu W, Beaudet A, Feller MB. Mice lacking specific
841 nicotinic acetylcholine receptor subunits exhibit dramatically altered spontaneous activity
842 patterns and reveal a limited role for retinal waves in forming ON and OFF circuits in the inner
843 retina. J Neurosci. 2000;20(20):7672-81.
844 34. Assali A, Gaspar P, Rebsam A. Activity dependent mechanisms of visual map formation--
845 from retinal waves to molecular regulators. Semin Cell Dev Biol. 2014;35:136-46.
846 35. Fassier C, Nicol X. Retinal Axon Interplay for Binocular Mapping. Front Neural Circuits.
847 2021;15:679440.

848 36. Faust TE, Gunner G, Schafer DP. Mechanisms governing activity-dependent synaptic
849 pruning in the developing mammalian CNS. Nat Rev Neurosci. 2021;22(11):657-73.
850 37. Rahman TN, Munz M, Kutsarova E, Bilash OM, Ruthazer ES. Stentian structural plasticity
851 in the developing visual system. Proc Natl Acad Sci U S A. 2020;117(20):10636-8.
852 38. Louail A, Sierksma MC, Chaffiol A, Baudet S, Assali A, Couvet S, et al. cAMP-Dependent
853 Co-stabilization of Axonal Arbors from Adjacent Developing Neurons. Cell Rep.
854 2020;33(1):108220.
855 39. Yasuda M, Nagappan-Chettiar S, Johnson-Venkatesh EM, Umemori H. An activity-
856 dependent determinant of synapse elimination in the mammalian brain. Neuron.
857 2021;109(8):1333-49 e6.
858 40. Munz M, Gobert D, Schohl A, Poquérusse J, Podgorski K, Spratt P, et al. Rapid Hebbian
859 axonal remodeling mediated by visual stimulation. Science. 2014;344(6186):904-9.
860 41. Koch SM, Dela Cruz CG, Hnasko TS, Edwards RH, Huberman AD, Ullian EM. Pathway-
861 specific genetic attenuation of glutamate release alters select features of competition-based
862 visual circuit refinement. Neuron. 2011;71(2):235-42.
863 42. Kutsarova E, Schohl A, Munz M, Wang A, Zhang YY, Bilash OM, et al. BDNF signaling in
864 correlation-dependent structural plasticity in the developing visual system. PLoS Biol.
865 2023;21(4):e3002070.
866 43. Ge X, Zhang K, Gribizis A, Hamodi AS, Sabino AM, Crair MC. Retinal waves prime visual
867 motion detection by simulating future optic flow. Science. 2021;373(6553).
868 44. Stellwagen D, Shatz CJ. An instructive role for retinal waves in the development of
869 retinogeniculate connectivity. Neuron. 2002;33(3):357-67.

870 45. Stellwagen D, Shatz CJ, Feller MB. Dynamics of retinal waves are controlled by cyclic
871 AMP. Neuron. 1999;24(3):673-85.
872 46. Sun C, Speer CM, Wang GY, Chapman B, Chalupa LM. Epibatidine application in vitro
873 blocks retinal waves without silencing all retinal ganglion cell action potentials in developing
874 retina of the mouse and ferret. J Neurophysiol. 2008;100(6):3253-63.
875 47. Zhang J, Ackman JB, Xu HP, Crair MC. Visual map development depends on the temporal
876 pattern of binocular activity in mice. Nat Neurosci. 2011;15(2):298-307.
877 48. Assali A, Le Magueresse C, Bennis M, Nicol X, Gaspar P, Rebsam A. RIM1/2 in retinal
878 ganglion cells are required for the refinement of ipsilateral axons and eye-specific segregation.
879 Sci Rep. 2017;7(1):3236.
880 49. Balice-Gordon RJ, Chua CK, Nelson CC, Lichtman JW. Gradual loss of synaptic cartels
881 precedes axon withdrawal at developing neuromuscular junctions. Neuron. 1993;11(5):801-15.
882 50. Gan WB, Lichtman JW. Synaptic segregation at the developing neuromuscular junction.
883 Science. 1998;282(5393):1508-11.
884 51. Wyatt RM, Balice-Gordon RJ. Activity-dependent elimination of neuromuscular
885 synapses. J Neurocytol. 2003;32(5-8):777-94.
886 52. Sanes JR, Lichtman JW. Development of the vertebrate neuromuscular junction. Annu
887 Rev Neurosci. 1999;22:389-442.
888 53. Buffelli M, Burgess RW, Feng G, Lobe CG, Lichtman JW, Sanes JR. Genetic evidence that
889 relative synaptic efficacy biases the outcome of synaptic competition. Nature.
890 2003;424(6947):430-4.

891 54. Balice-Gordon RJ, Lichtman JW. Long-term synapse loss induced by focal blockade of
892 postsynaptic receptors. Nature. 1994;372(6506):519-24.
893 55. Kopp DM, Perkel DJ, Balice-Gordon RJ. Disparity in neurotransmitter release probability
894 among competing inputs during neuromuscular synapse elimination. J Neurosci.
895 2000;20(23):8771-9.
896 56. Kleindienst T, Winnubst J, Roth-Alpermann C, Bonhoeffer T, Lohmann C. Activity-
897 dependent clustering of functional synaptic inputs on developing hippocampal dendrites.
898 Neuron. 2011;72(6):1012-24.
899 57. Lee KF, Soares C, Thivierge JP, Beique JC. Correlated Synaptic Inputs Drive Dendritic
900 Calcium Amplification and Cooperative Plasticity during Clustered Synapse Development.
901 Neuron. 2016;89(4):784-99.
902 58. Winnubst J, Cheyne JE, Niculescu D, Lohmann C. Spontaneous Activity Drives Local
903 Synaptic Plasticity In Vivo. Neuron. 2015;87(2):399-410.
904 59. Niculescu D, Michaelsen-Preusse K, Guner U, van Dorland R, Wierenga CJ, Lohmann C. A
905 BDNF-Mediated Push-Pull Plasticity Mechanism for Synaptic Clustering. Cell Rep.
906 2018;24(8):2063-74.
907 60. Kirchner JH, Gjorgjieva J. Emergence of local and global synaptic organization on cortical
908 dendrites. Nat Commun. 2021;12(1):4005.
909 61. Chung WS, Clarke LE, Wang GX, Stafford BK, Sher A, Chakraborty C, et al. Astrocytes
910 mediate synapse elimination through MEGF10 and MERTK pathways. Nature.
911 2013;504(7480):394-400.

912 62. Schafer DP, Lehrman EK, Kautzman AG, Koyama R, Mardinly AR, Yamasaki R, et al.
913 Microglia sculpt postnatal neural circuits in an activity and complement-dependent manner.
914 Neuron. 2012;74(4):691-705.
915 63. Stevens B, Allen NJ, Vazquez LE, Howell GR, Christopherson KS, Nouri N, et al. The
916 classical complement cascade mediates CNS synapse elimination. Cell. 2007;131(6):1164-78.
917 64. Burbridge TJ, Xu HP, Ackman JB, Ge X, Zhang Y, Ye MJ, et al. Visual circuit development
918 requires patterned activity mediated by retinal acetylcholine receptors. Neuron.
919 2014;84(5):1049-64.
920 65. Picciotto MR, Zoli M, Lena C, Bessis A, Lallemand Y, Le Novere N, et al. Abnormal
921 avoidance learning in mice lacking functional high-affinity nicotine receptor in the brain.
922 Nature. 1995;374(6517):65-7.
923 66. Paxinos G. Atlas of the developing mouse brain at E17.5, P0 and P6. 1st ed. Amsterdam ;
924 Boston: Elsevier; 2007. xi, 353 p. p.
925 67. Babcock H, Sigal YM, Zhuang X. A high-density 3D localization algorithm for stochastic
926 optical reconstruction microscopy. Optical Nanoscopy. 2012;1(6).
927 68. Babcock HP, Huang F, Speer CM. Correcting Artifacts in Single Molecule Localization
928 Microscopy Analysis Arising from Pixel Quantum Efficiency Differences in sCMOS Cameras. Sci
929 Rep. 2019;9(1):18058.
930
931

Supporting information

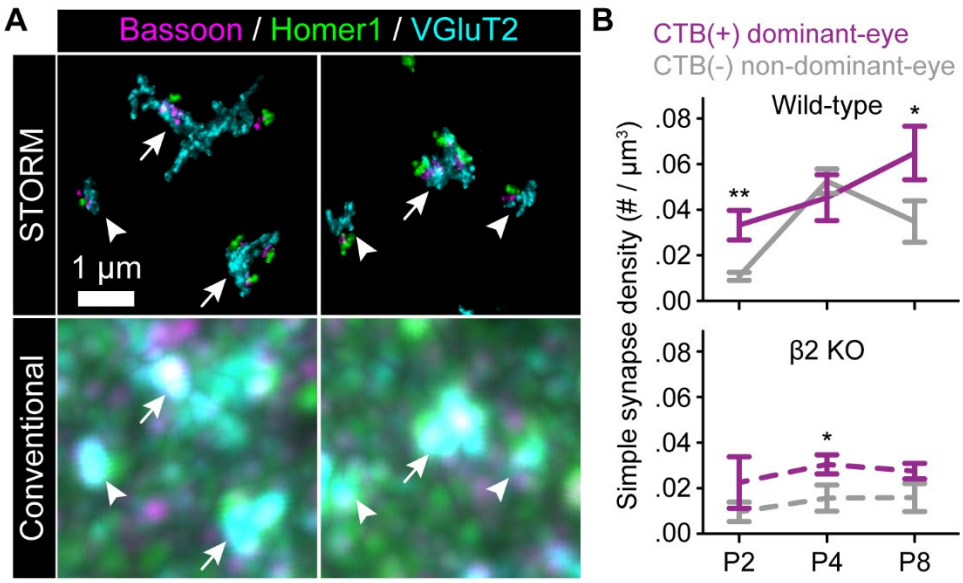

S1 Fig. Eye-specific differences in simple synapse density in the first postnatal week, related to Fig 1. (A) Volumetric STORM imaging enables the differentiation of complex (arrows) versus simple (arrowheads) synapses (top panels), which cannot be distinguished in diffraction-limited conventional images (bottom panels). (B) The density of eye-specific simple synapses across ages in WT (top panel) and β2 KO mice (bottom panel). Error bars represent means ± SEMs (N=3 biological replicates for each age/genotype). Statistical tests were performed using a one-way ANOVA. *: P<0.05. **: p<0.01.

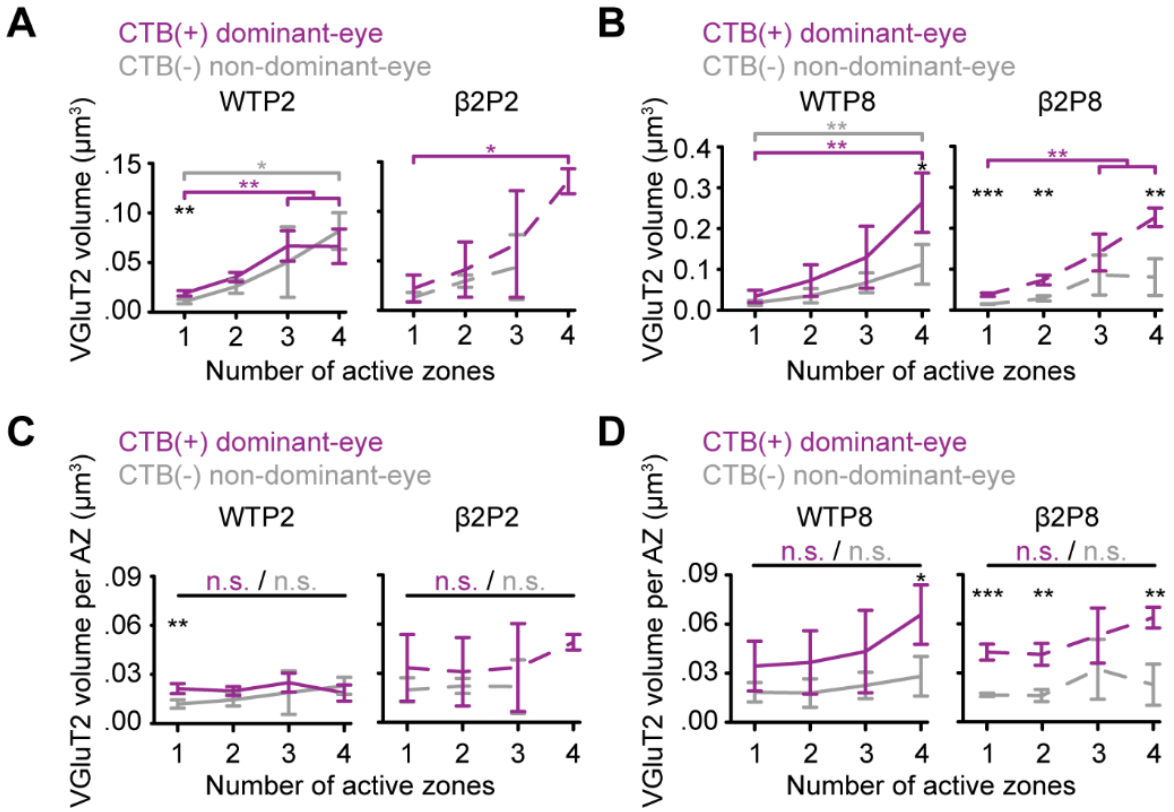

S2 Fig. Complex synapses undergo eye-specific vesicle pool maturation, related to Fig 2. (A-B) VGluT2 cluster volume relative to AZ number for each synapse in WT (left panels) and β2KO mice (right panels) at P2 (A) and P8 (B). Error bars indicate means ± SEMs (N=3 biological replicates for each age and genotype). A one-way ANOVA was used to assess statistical significance between eye-of-origin (black asterisks) and eye-specific synapses with different AZ numbers (colored asterisks). A post hoc Tukey's test was conducted for pairwise comparisons between simple (1 AZ) and complex (>1 AZ) synapses. (C-D) VGluT2 volume per AZ (bassoon cluster) for all synapses in WT (left panels) and β2KO mice (right panels) at P2 (C) and P8 (D). Figure presentation and statistical tests were the same as shown in (A) and (B). In all panels: *: $p<0.05$; **:$p<0.01$; ***:$p<0.001$.

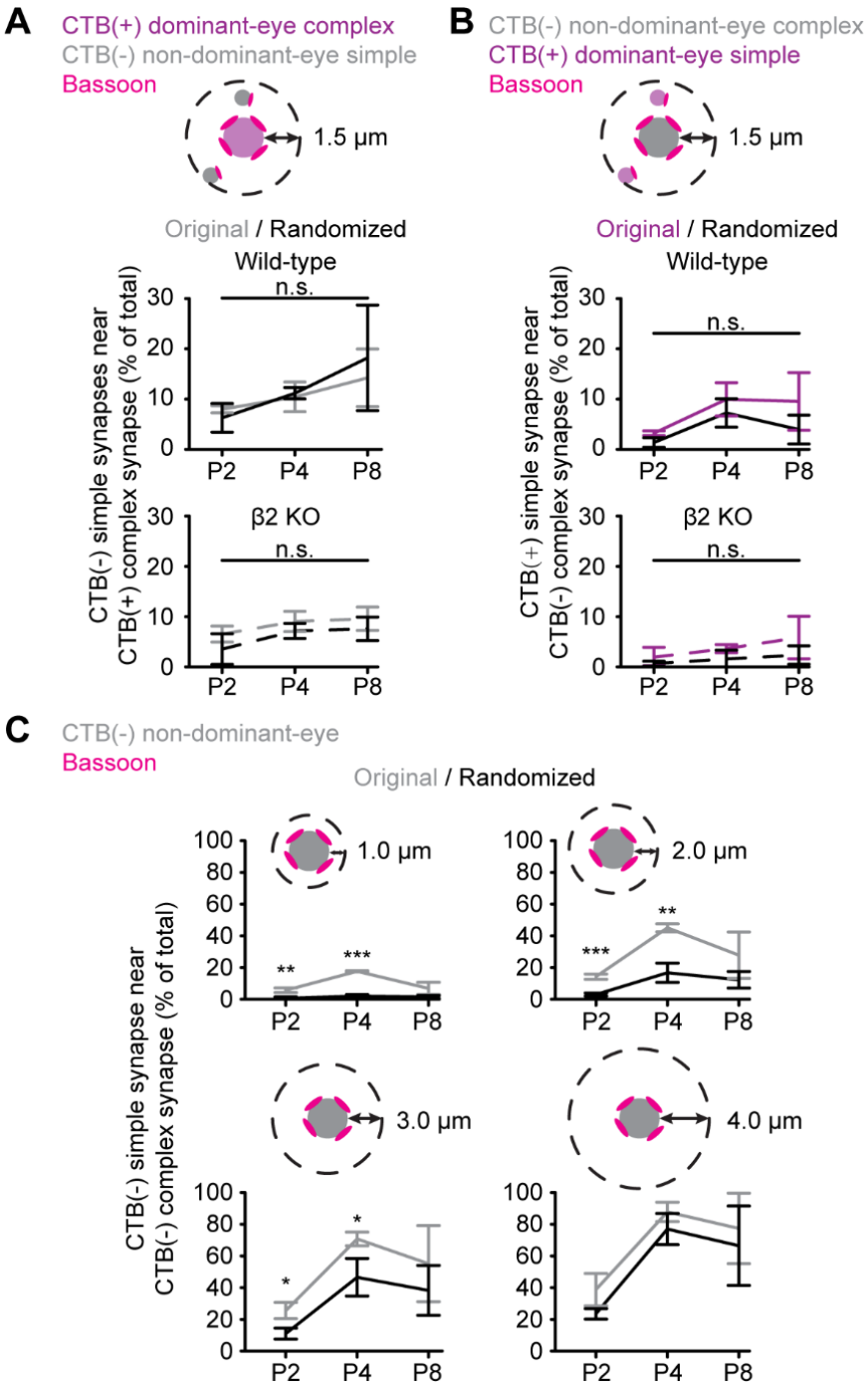

S3 Fig. Complex synapses are loci for synaptic clustering, related to Fig 3. (A) Percentage of CTB(-) non-dominant-eye simple synapses near an opposite-eye complex synapse in WT (top panel) and β2KO mice (bottom panel). (B) Same presentation as in (A), showing percentage of CTB(+) dominant-eye simple synapses

961 near an opposite-eye complex synapse. (C) To further validate our selection of a 1.5 um
962 search radius, we performed additional control measurements with varying local search
963 radii. For complex synapses of both eyes-of-origin, the detection of non-random
964 clustering increased when the search radius was expanded from 1 μm to 2 μm and then
965 decreased as the radius was further expanded to sample the average simple synapse
966 density (3-4 μm) (example with CTB(-) non-dominant-eye synapses). The figure shows
967 the percentage of CTB(-) non-dominant-eye simple synapses near like-type CTB(-)
968 complex synapses across development as a function of increasing distance cutoffs from
969 the surface of complex synapses. Distributions are shown for cutoff distances of 1.0 μm
970 (top left panel), 2.0 μm (top right panel), 3.0 μm (bottom left panel), and 4.0 μm (bottom
971 right panel). For all panels, grey and purple lines represent the original data, and black
972 lines represent the results from a randomized simple synapse distribution. Error bars
973 represent means ± SEMs (N=3 biological replicates for each age and genotype).
974 Statistical tests between original and randomized data were performed using one-way
975 ANOVA. *: $P<0.05$; **: $p<0.01$; ***: $p<0.001$. “n.s.” indicates no significant differences.
976
977

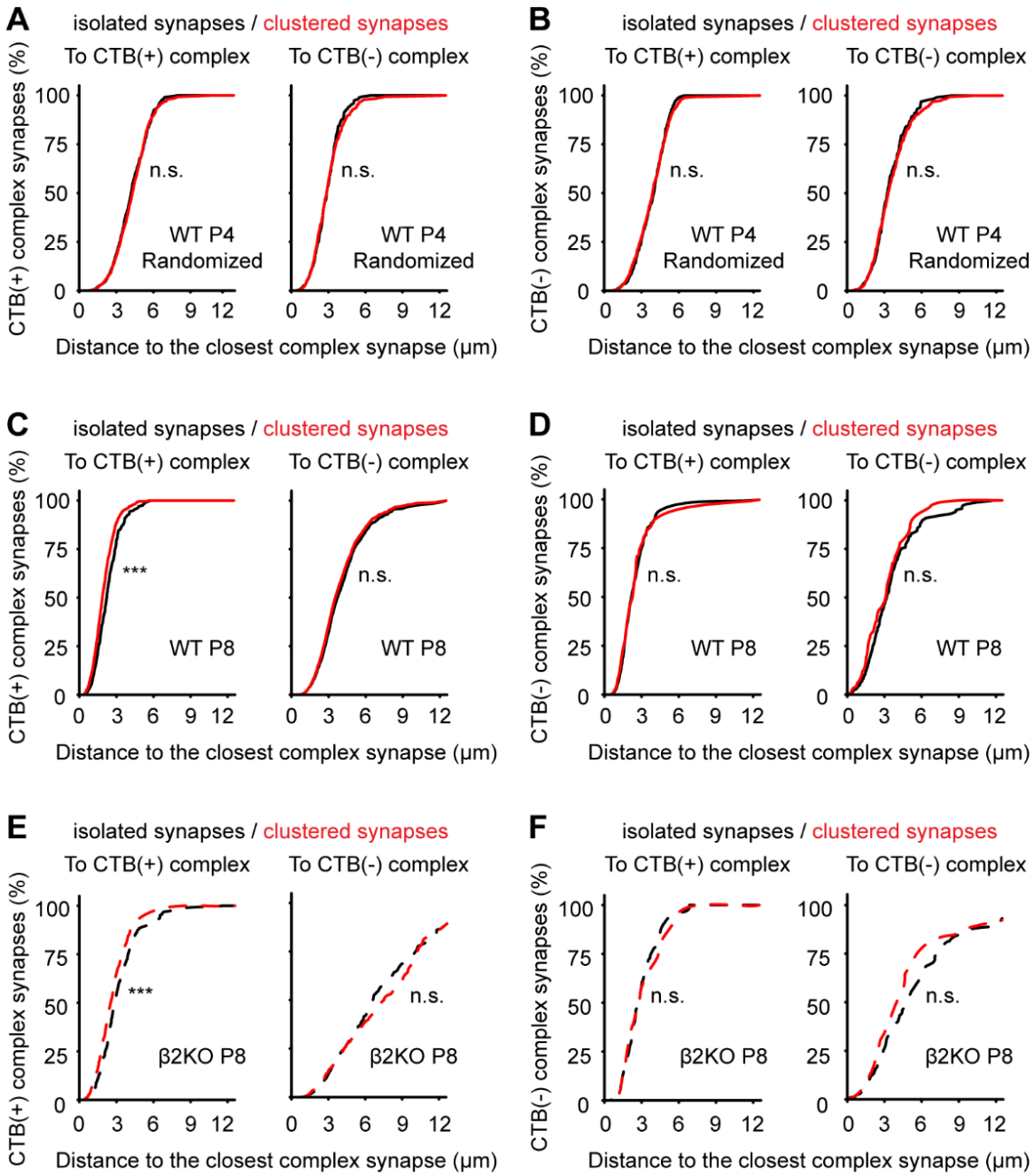

S4 Fig. Complex synapses mediate distance-dependent synaptic stabilization and punishment underlying eye-specific competition, related to Fig. 4. (A) Cumulative histogram of the distances from CTB(+) complex synapses to their nearest CTB(+) (left panel) and CTB(-) (right panel) complex synapse in P4 WT data where simple synapse distributions were randomized. Black lines show distributions for isolated complex

984 synapses with no nearby (<1.5 μm) simple synapses and red lines show distributions for
985 clustered complex synapses with one or more simple synapses nearby. (B) Same
986 presentation as in (A), showing distances from CTB(-) complex synapses to their
987 nearest CTB(+) (left panel) and CTB(-) (right panel) complex synapse in P4 WT
988 randomized data. (C and D) Same presentation as in A/B, showing WT P8 original data.
989 (E and F) Same presentation as in C/D, showing β2KO P8 original data. Nonparametric
990 Kolmogorov-Smirnov tests were used for statistical comparisons (N=3 biological
991 replicates for each condition). ***: $p<0.001$. "n.s." indicates no significant differences.
992